The Thermally Driven Ocean Circulation with Realistic Bathymetry

ADA GJERMUNDSEN, JOSEPH H. LACASCE, AND LIV DENSTAD[a]

Department of Geosciences, University of Oslo, Oslo, Norway

(Manuscript received 19 July 2017, in final form 19 January 2018)

ABSTRACT

The global circulation driven solely by relaxation to an idealized surface temperature profile and to interior mixing is examined. Forcing by winds and evaporation/precipitation is excluded. The resulting circulation resembles the observed in many ways, and the overturning is of similar magnitude. The overturning is driven by large-scale upwelling in the interior (which is relatively large, because of the use of a constant mixing coefficient). The compensating downwelling occurs in the northern North Atlantic and in the Ross and Weddell Seas, with an additional, smaller contribution from the northern North Pacific. The latter is weaker because the Bering Strait limits the northward extent of the flow. The downwelling occurs in frictional layers near the boundaries and depends on the lateral shear in the horizontal flow. The shear, in turn, is linked to the imposed surface temperature gradient via thermal wind, and as such, the downwelling can be reduced or eliminated in selected regions by removing the surface gradient. Doing so in the northern North Atlantic causes the (thermally driven) Antarctic Circumpolar Current to intensify, increasing the sinking along Antarctica. Eliminating the surface gradient in the Southern Ocean increases the sinking in the North Atlantic and Pacific. As there is upwelling also in the western boundary currents, the flow must increase even more to accomplish the necessary downwelling. The implications of the results are then considered, particularly with respect to Arctic intensification of global warming, which will reduce the surface temperature gradient.

1. Introduction

The buoyancy-driven circulation (BDC) is central to the climate system. It is responsible for a substantial fraction of the global heat transport and for the sequestration of CO_2 to the abyss, where it resides for hundreds to thousands of years. The BDC, however, is a complex system. With deep western boundary currents, distributed (and poorly characterized) regions of upwelling and downwelling, and complex interbasin connections, the BDC defies simple characterizations (e.g., Bryan 1987; Colin de Verdière 1988; Marotzke 1997).

Atmospheric heat transport acts to reduce the latitudinal surface temperature gradient imposed by solar heating (e.g., Marshall and Plumb 2007). This temperature gradient also impacts the ocean, as it is associated with surface zonal shear due to the thermal wind relation. Other mechanisms affect the surface density, such as evaporation/precipitation and ice melt, but surface heating is large scale and, excluding seasonal variations, relatively constant. Nevertheless, thermal forcing is often overlooked in favor of wind forcing (Toggweiler and Samuels 1995; Gnanadesikan and Hallberg 2000; Nikurashin and Vallis 2012; Marshall and Speer 2012).

It is well known that the extent to which surface temperature forcing affects the circulation depends on vertical mixing. In the absence of mixing, the BDC would be confined to a vanishingly shallow surface layer, and cold, downwelled waters would fill the abyss (Sandström 1908; Paparella and Young 2002). Thus, wind- and tidal-induced stirring is required for the downward penetration of the thermocline (Hughes et al. 2009; Saenz et al. 2012). The tides by themselves have little direct impact on the large-scale overturning (Munk and Wunsch 1998; Waterhouse et al. 2014), but the winds certainly do, affecting the direction and strength of flow in the western boundary currents (WBCs) and driving overturning in the Southern Ocean via Ekman suction. Indeed, the latter has been cited as a principal cause of global overturning (e.g., Toggweiler and Samuels 1995; Gnanadesikan and Hallberg 2000; Nikurashin and Vallis 2012; Marshall and Speer 2012).

But how much of the observed circulation can be accounted for without wind forcing? Excluding winds is

[a] Current affiliation: Meteorologisk Institutt, Oslo, Norway.

Corresponding author: Ada Gjermundsen, ada.gjermundsen@geo.uio.no

DOI: 10.1175/JPO-D-17-0147.1

easily done with models, as the vertical mixing is imposed rather than generated by the winds and tides. This is not as unusual as it sounds, since tides are not simulated in climate models, but tidal mixing is retained. Nevertheless, the global BDC has been studied only rarely in the absence of wind forcing.

Knowing how thermal forcing affects the overturning is important for a number of reasons: for example, when assessing how the ocean will to respond to climate change. Preferential warming in the Arctic, with the associated loss of sea ice and snow cover, will alter the surface temperature gradient in the Northern Hemisphere (NH) (Serreze and Francis 2006; Screen and Simmonds 2010). But the importance of this contribution in particular, compared to changes in freshwater input from glacial melting or in wind forcing, is not known.

Much of our understanding about the BDC comes from idealized models, both theoretical and numerical (e.g., Robinson and Stommel 1959; Pedlosky 1969; Bryan 1987; Colin de Verdière 1988; Marotzke 1997; Huck et al. 1999; Marotzke and Scott 1999; Park and Bryan 2000, 2001; Huck and Vallis 2001; LaCasce 2004; Pedlosky and Spall 2005; Park 2006; Schloesser et al. 2012; Gjermundsen and LaCasce 2017, hereinafter GL17). Such studies are directly relevant here and are discussed further in section 3. Simulations with realistic bathymetry are far fewer (Cox 1989; England 1993; Cai 1994; Cai and Baines 1996; Saenko et al. 2002). Cai (1994) and Cai and Baines (1996) used coarse-resolution ocean models to this end, relaxing the surface temperature and salinity to observed values. The resulting circulation resembled that in the ocean in many ways, with intensified WBCs, deep water formation in the northern North Atlantic and in the Ross and Weddell Seas, and a realistic overturning. Saenko et al. (2002) also examined the BDC, using a fully coupled climate model, and found that thermal forcing is the main driver of the Atlantic overturning, with haline forcing playing a secondary role. But while such studies indicate that thermal forcing is important, the detailed aspects of the circulation were not fully examined.

Here, we study the steady BDC using a globally configured general circulation model, forced solely by an idealized surface temperature profile. The latter is hemispherically and zonally symmetric to mimic solar heating alone (using observed surface temperatures is less desirable, as those are affected by ocean heat transport).

The resulting circulation bears many similarities to the observed. It also resembles the flow observed in the idealized studies, meaning those can be used to understand certain aspects, like the downwelling. Furthermore, excluding wind forcing greatly facilitates diagnosing the complex interbasin exchanges.

The model and experimental setup are discussed first. Then, we examine the response, including the interbasin exchange. To isolate the overturning associated with the overturning in the Northern and Southern Hemispheres, we examine additional experiments in which the surface forcing is altered in each. Last, we discuss the implications and directions for future work.

2. Model description

We use the Massachusetts Institute of Technology general circulation model (MITgcm) (Marshall et al. 1997a,b) in an ocean-only configuration, with no sea ice. The resolution is $1° \times 1° \cos(\theta)$ horizontally (where θ is latitude), with 24 vertical levels spanning 6 km. The vertical resolution is 20 m in the upper layers, increasing to 900 m at depth. Global ETOPO1 (Amante and Eakins 2008) bathymetry was also used, interpolated to the model grid. The surface temperature was relaxed to a zonally uniform profile, given by $27\cos(\theta)$, with a restoring time scale of 1 month. The salinity was kept constant, and no freshwater forcing was applied, so buoyancy is determined solely by temperature.

Isopycnal mixing is parameterized as per the scheme of Gent and Mcwilliams 1990 (GM) with a transfer coefficient of $1000\,\mathrm{m^2\,s^{-1}}$ in the horizontal. An additional simulation with a constant lateral diffusivity was run for comparison. A constant background vertical diffusivity $\kappa_v = 10^{-4}\,\mathrm{m^2\,s^{-1}}$ was also used, comparable to the globally averaged estimate (Munk 1966; Waterhouse et al. 2014). We conducted an additional run with $\kappa_v = 5 \times 10^{-5}\,\mathrm{m^2\,s^{-1}}$, and those results are also discussed below. Convection is represented through enhanced vertical mixing, in which the vertical mixing is increased to $10\,\mathrm{m^2\,s^{-1}}$ under unstable conditions (Klinger et al. 1996).

3. Results from idealized models

As noted, the BDC has been studied extensively using models with idealized geometry, often in a single hemisphere. GL17 is one example, and they used forcing like that in the present study. The solution with realistic bathymetry shows numerous similarities with the simulations of GL17, so a short summary of their findings is given here for comparison.

The surface flow in the GL17 solution is shown in Fig. 1. The flow in the interior is eastward in thermal wind balance with the imposed surface temperature gradient (Fig. 1, upper panel). The velocities are largest in the north and weaker in the south. There is a WBC as well, which flows north and feeds the interior. The WBC is supplied by a current along the southern boundary.

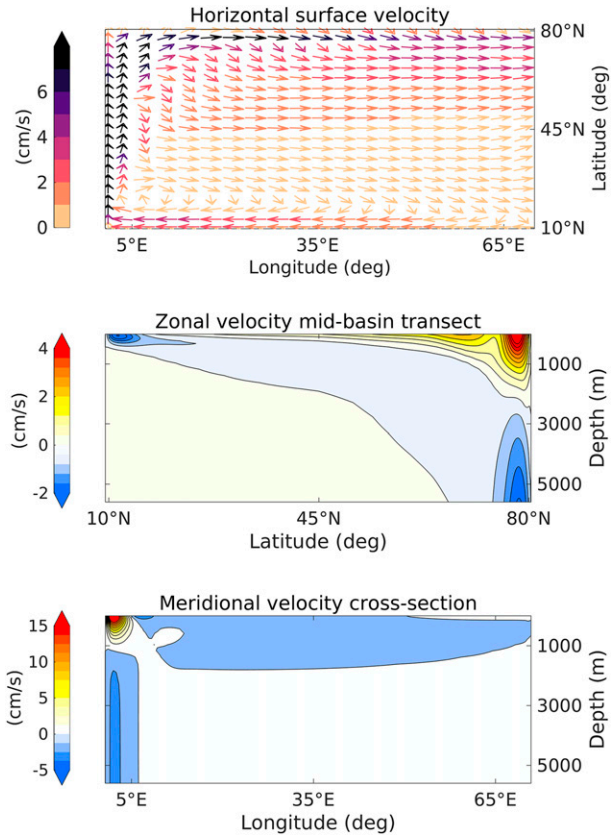

FIG. 1. Velocity figures from a square basin simulation using the same temperature forcing as in this study. (top) Horizontal velocity at the surface. The arrows indicate the direction, and the colors indicate the strength of the flow. (middle) Midbasin transect (35°E) of the zonal velocity. (bottom) Midbasin cross section (45°N) of the meridional velocity.

In the vertical (middle panel), the interior surface flow is eastward, and there is weaker westward flow at depth. The latter cancels the former in a vertical integral, as there is no barotropic flow with buoyancy forcing and a flat bottom (e.g., Colin de Verdière 1988). The westward flow surfaces in the south, constituting the current feeding the WBC noted above. In the north, the zonal flow extends to the bottom; this is due to convection homogenizing the water column (GL17).

The WBC has a simple baroclinic structure with two cores (lower panel). The surface flow is northward, and the deeper flow, the model's deep WBC, is to the south. The surface core turns east at the northern wall and proceeds to the eastern wall (upper panel), where it downwells. The returning westward flow then feeds the deep WBC. As such, the abyssal circulation resembles that envisioned by Stommel and Arons (1959). The vertical velocity is also similar (GL17), being largely uniform and upward in the interior.

4. Results: Description of the control run

Shown in the right panel of Fig. 2 are temperature transects from the global run from the Atlantic, Indian, and Pacific Oceans, respectively. The upper ocean is stably stratified with a thermocline extending to roughly 800-m depth, while the abyss is weakly stratified. The latter mostly comprises the model's Antarctic Bottom Water (AABW). At high latitudes, where convection is active, the temperature is nearly homogeneous. This is especially evident close to Antarctica.

The profiles are reasonably realistic, as can be seen when comparing to similar transects calculated with data from the *World Ocean Atlas* (*WOA*) (Locarnini et al. 2013) (Fig. 2, left column). Note, though, the AABW is approximately 6°C warmer in the MITgcm simulation because of the relaxation temperature, which is 7°C at 75°S. The SSTs in *WOA* are nearer to −1.5°C. Thus, the surface temperature gradients in *WOA* are stronger than those simulated here. This implies that the thermal wind shear in our simulations is somewhat less than in reality at high latitudes. Note, too, that the *WOA* thermocline is undulating, and the isopycnals outcrop in sharp frontal zones in the Southern Ocean; this is due to wind forcing (excluded in the MIT simulation). But otherwise, the large-scale structure is similar.

a. *Horizontal velocity fields*

The horizontal velocities are plotted in Figs. 3 and 4. Away from continental boundaries and the equator, the surface flow in the interior is eastward and intensified at high latitudes (Fig. 3). There are WBCs in all the basins, feeding the interior flow, and most of the WBCs flow poleward and are fed by equatorial flows that intensify from east to west. All these features have counterparts in the square basin simulations. The exception is the Southern Ocean. The eastward flow there constitutes the model's ACC, which is solely thermally forced. The current proceeds with relatively little meridional deviation around Antarctica.

At 1200 m, the WBCs in the North Pacific and North Atlantic are reversed, being southward (Fig. 4, upper panel). In the North Pacific, the WBC feeds an eastward flow along the equator, but the deep WBC in the Atlantic Ocean crosses the equator and eventually joins the ACC, which is still eastward at this depth. However, there is westward flow to the north of the ACC, in the South Pacific, which starts just west of Drake Passage. This flow splits east of New Zealand, with a portion flowing south to rejoin the ACC and the rest continuing westward, south of Australia and into the Indian Ocean.

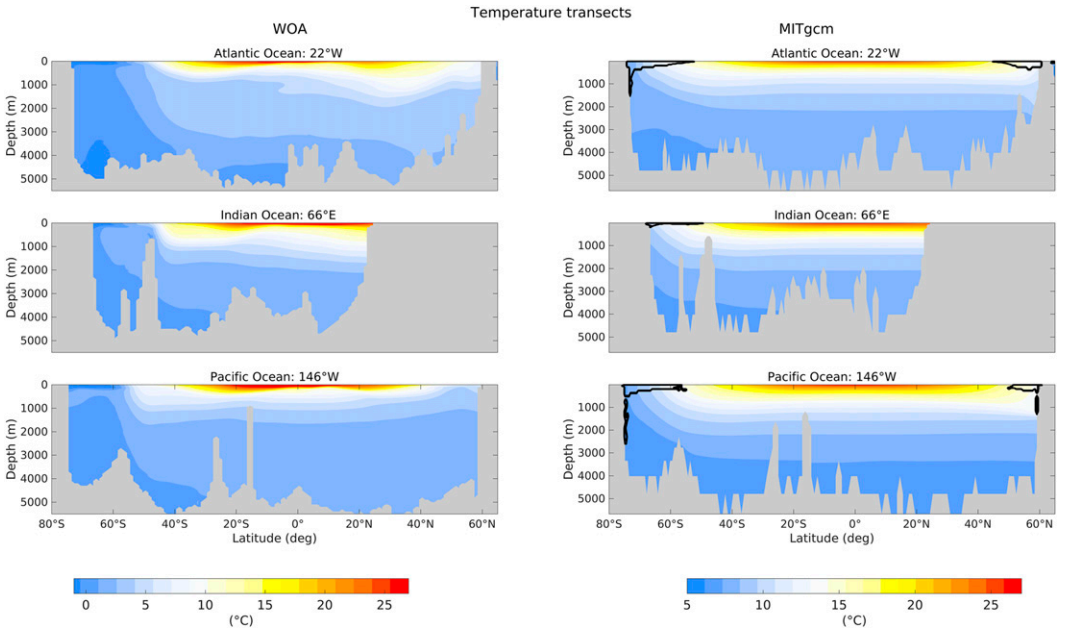

FIG. 2. Potential temperature transects of the (top) Atlantic (22°W), (middle) Indian (66°E), and (bottom) Pacific (146°W) Oceans from the (left) *WOA* (Locarnini et al. 2013) and (right) MITgcm. The black lines show areas where the convective index is greater than zero in the MITgcm simulation; that is, the vertical diffusivity is large due to enhanced mixing.

At 1900 m (Fig. 4, middle panel), the flow in the Northern Hemisphere is weak, except for the Atlantic WBC, the model's North Atlantic Deep Water (NADW). This current is thus deeper than the corresponding WBC in the Pacific. The NADW proceeds along the length of the Atlantic basin, joining the ACC. The latter is still eastward at this depth, but also narrower than at the shallower depths. The westward flow in the South Pacific is present as well, but weaker. The flow at 3300 m (Fig. 4, bottom panel) is dominated by bottom currents originating from the Ross and Weddell Seas. These currents flow primarily beside ridges into the other basins, weakening along the way because of mixing.

The vertical extent of the ACC is seen in the zonal transects in Fig. 5. The current is strongest in the upper 2000 m but reaches the bottom in some regions. The transport in Drake Passage is 104 Sv ($1\,\text{Sv} \equiv 10^6\,\text{m}^3\,\text{s}^{-1}$), a significant fraction of the observed value (from 137 to 173 Sv; Cunningham et al. 2003; Meredith et al. 2011; Donohue et al. 2016). In the basins, the shallow flow is eastward and deepens from the tropics to the poles, and the flow beneath is westward, as in the square basin (Fig. 1, middle panel). However, the flow is confined to the upper 2500 m; in the square basin simulation, the flow in the convective region extended to the bottom (5600 m). The shallower extent here is due to bathymetry limiting the depth of downwelling (e.g., Park and Bryan 2000).

Interestingly, there are also alternating zonal jets at the equator. The most significant is an eastward jet, reminiscent of the Equatorial Undercurrent. This shallows to the east and is therefore not visible in the eastern basin at 1200 m (Fig. 4). Similar jets are present in the Atlantic and Indian Oceans, but the Pacific undercurrent is the most pronounced. Stacked jets are a well-known feature of the equatorial Pacific (Picaut and Tournier 1991; Hua et al. 1997; Ménesguen et al. 2009), but it is notable that they are obtained here with only buoyancy forcing.

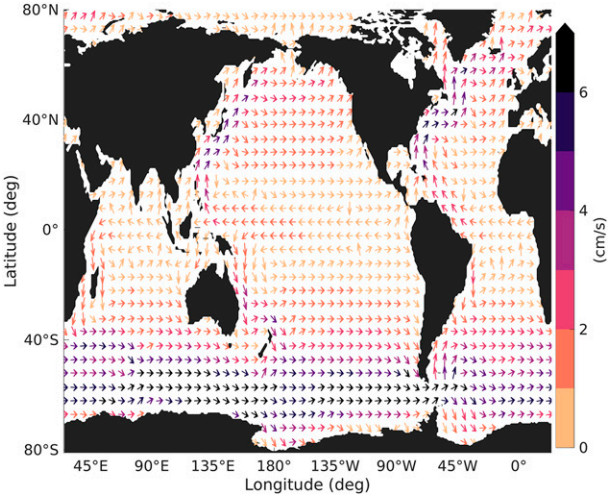

FIG. 3. Horizontal velocity at the surface. The arrows indicate the direction and the colors indicate the strength of the flow.

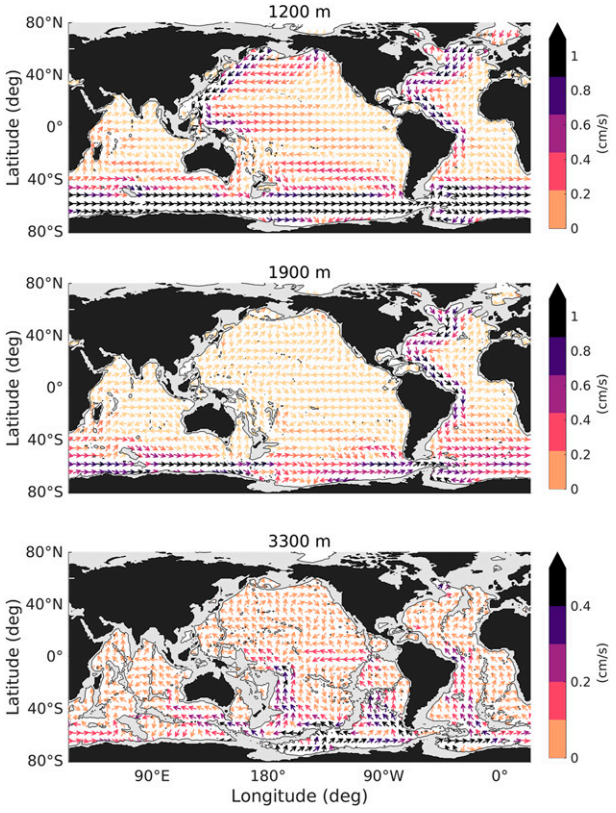

FIG. 4. Horizontal velocity at (top) 1200, (middle) 1900, and (bottom) 3300 m. The arrows indicate the direction and the colors indicate the strength of the flow. Note that the color bars differ.

The vertical structure of the WBCs differs significantly among the basins (Fig. 6). At 30°N, the WBCs flow north at the surface and south at depth, as in the square basin. The structures in the North Pacific and North Atlantic are similar, but the deep WBC in the Atlantic is stronger and deeper. At the equator, the WBCs in the Pacific are relatively weak, implying limited exchange with the other basins. In the Indian Ocean, the surface WBC, the simulation's Agulhas Current, flows southward, and there is a northward flow beneath. So there is exchange between the northern Indian Ocean and other basins. The notable case though is the Atlantic, which has three alternating cores at the equator. The surface one flows north, the middle (the NADW) flows south, and the bottom, a portion of the AABW, is northward. These reflect the significant interbasin exchange with the North Atlantic.

The southward-flowing Agulhas Current is also evident at 30°S. There is also a double core of southward flow in the western Pacific, east of Australia and New Zealand respectively; these are related to the westward flow north of the ACC mentioned earlier. In contrast, there are four WBC cores in the Atlantic. The surface core is poleward and forced locally in the South Atlantic, while the second feeds the northward surface flow at the equator and originates primarily in the ACC. The third is the NADW, feeding the ACC, and the deepest, at 4000 m, is the northward-flowing AABW. Similar northward bottom currents are evident in all basins.

b. *The overturning circulation*

The cells of the meridional overturning circulation (MOC) are shown in Fig. 7. These are calculated by vertically integrating the meridional velocity in z coordinates.[1] Though a drastic simplification of the 3D circulation, the cells highlight some differences. For one, the strength of the northern overturning cells is related to the basin geometry. The Atlantic overturning, at 17 Sv, is the strongest cell in the NH because the basin extends farthest north. The Pacific basin, bounded at 64°N, has weaker cell (10 Sv) confined to north of the equator. And the Indian basin, bounded at 25°N, has essentially no northern cell. In the south, the AABW cell is present in all three basins (as the southern boundary, Antarctica, occupies roughly the same range of latitudes in the basins). The cell is most pronounced in the Pacific, however, the widest of the three basins.

The global overturning cells are shown in the upper-left panel of Fig. 8. The northern and southern cells have comparable amplitudes, roughly 25 Sv. The northern cell is limited to the upper 2000 m and closes north of the equator (the NADW, which extends farther south, is obscured in the global zonal integral). The southern cell extends to the bottom and actually comprises two subcells. The northern cell is north of 60°S, where continents block the latitude lines. The southern cell is associated with downwelling and upwelling in the Ross and Weddell Seas, as seen next. The two subcells join in the Drake Passage latitudes. The deep, northward-flowing branch is the AABW. The shallower branch displays a prominent dip to below 1000 m. This follows because zonally averaged meridional flow is only possible below the sill depth (Gill and Bryan 1971; Toggweiler and Samuels 1995; Warren et al. 1996). A substantial fraction of the southward flow occurs just east of the Kerguelen Plateau, in a broad core from 1000- to 2000-m depth (not shown).

Figure 9 shows the important locations for vertical transport. Here, we distinguish the western boundary

[1] The overturning streamfunction can also be calculated in density coordinates, which is more representative of fluid parcel motion (e.g., Döös and Webb 1994; Vallis 2006). We use z coordinates here, for reference with the bottom depth and for comparison with the idealized models, but a description of the overturning in temperature coordinates is included in the appendix.

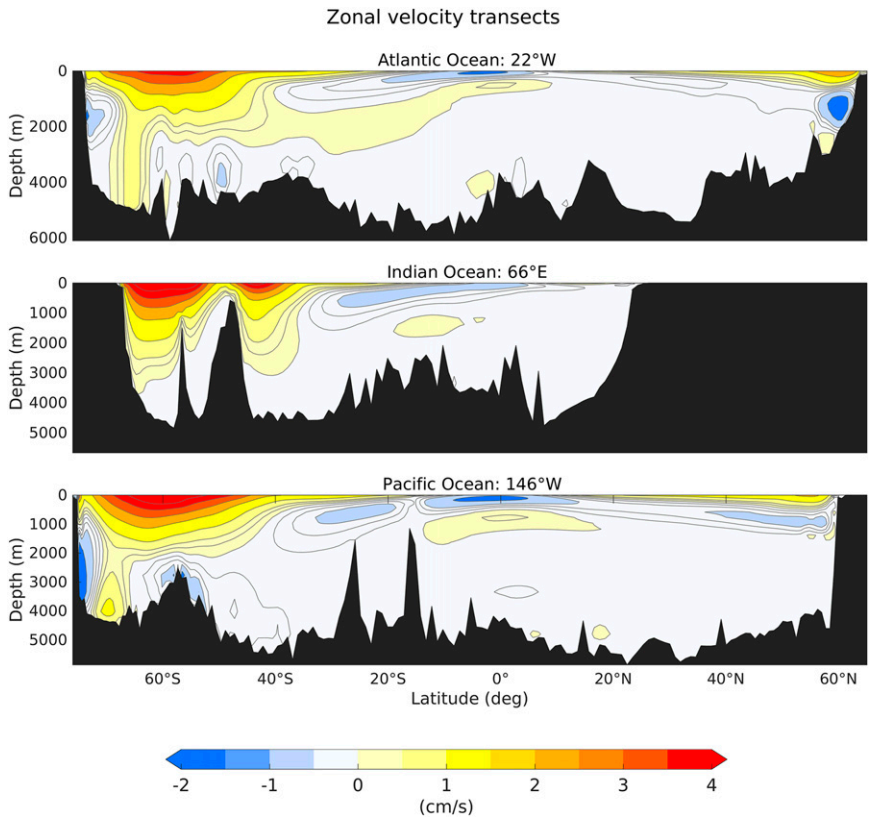

FIG. 5. Zonal velocity transects of the Atlantic (22°W), Indian (66°E), and Pacific (146°W) Oceans (i.e., the same transects as shown in Fig. 2).

regions, defined by the lateral extent of the surface WBCs, and the interiors. The depths differ and were chosen based on the vertical structure of the WBCs, the ACC, and the MOC. Broadly speaking, there is upwelling over much of the interior and in the WBCs, while downwelling occurs near the boundaries at high latitudes.

In the Atlantic, the upwelling in the interior and in the WBCs is of similar magnitude (5–6 Sv). The sinking occurs primarily in the Labrador and Irminger Seas and in the Icelandic basin. There is additional sinking in the Nordic Seas, but the inflow is less than the observed, probably because of model resolution. The total downwelling in the region is about 17 Sv, a value greater than the total upwelling in the North Atlantic. The residual is supplied by the cross-equatorial surface flow in the WBC, noted earlier. About 50% of the NADW upwells north of the equator, and an additional 25% upwells in the South Atlantic. The remaining 4 Sv is exported to the Southern Ocean.

In the North Pacific, 10 Sv downwells, mostly in the northeast. As the sinking occurs at a relatively low latitude, the downwelled waters are warmer and sink less than in the North Atlantic. In addition, the interior upwelling is much greater because the basin is wider. As such, all of the downwelled water returns to the surface north of the equator. The Pacific overturning is thus confined to the North Pacific (Fig. 7, middle panel).

The Southern Ocean is the most complex region, with areas of upwelling and downwelling over much of the region. However, the major sites of AABW formation are the Ross Sea and the Weddell Sea. More than half of the AABW upwells along the slopes of Antarctica, as inferred from the global MOC (Fig. 8, upper-left panel). The rest of the AABW proceeds northward into the basins. In total, 21 Sv of AABW water enters the Pacific and the Indian Oceans, while 6 Sv flows from the Weddell Sea into the Atlantic. The waters upwell in the interiors and in the WBCs and return.

5. Altering the northern sinking

The Atlantic and Pacific overturning cells differ in both extent and strength. To make them more equivalent, we altered the temperature forcing in the North Atlantic by keeping the relaxation temperature constant north of 64°N (i.e., the latitude of the Bering Strait) (Fig. 10, top panel). This is similar to what happens when the region is covered by sea ice, although the surface temperature here is above freezing. Note that this

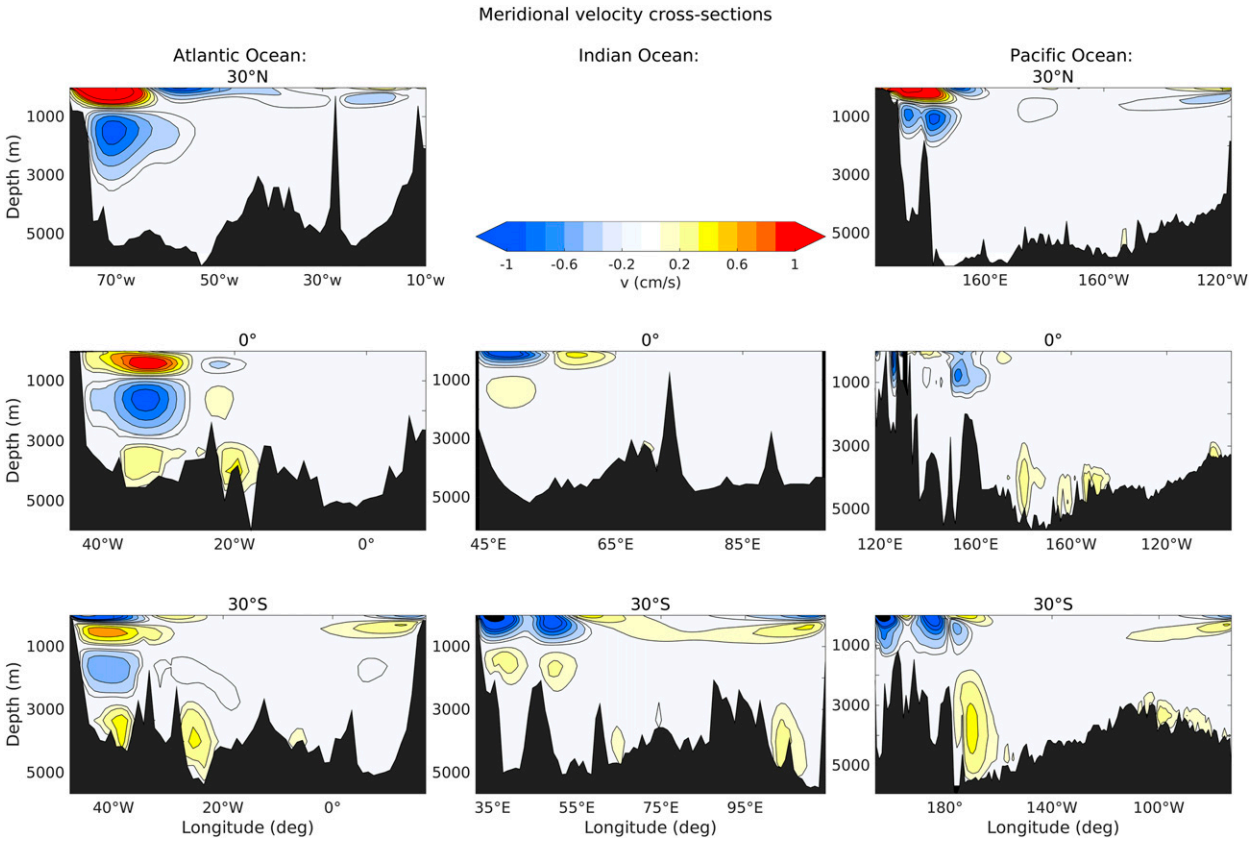

FIG. 6. Cross sections of the meridional velocity at (top) 30°N, (middle) 0°, and (bottom) 30°S for the (left) Atlantic Ocean, (center) Indian Ocean, and (right) Pacific Ocean.

profile does not preclude flow or convection north of 64°N; it simply eliminates the induced zonal shear.

The surface flow (Fig. 10, upper panel) changes little from the control run. Despite there being no forced zonal flow in the Nordic Seas, there is still inflow from south of Iceland. But the sinking in the Nordic Seas is reduced, as there is no longer flow toward Norway. Instead, the sinking is primarily south of Iceland, and the downwelled waters are correspondingly warmer. The result is that the Atlantic MOC weakens (to 13 Sv) and is confined to the upper 2000 m. The cell also extends only to 15°S because the upwelling in the interior and in the WBC, which is nearly the same as before, is sufficient to close the overturning.

Significantly, both the AABW and the ACC strengthen when the Atlantic MOC weakens. The AABW increases by 1 Sv, and the transport in Drake Passage increases to 112 Sv, that is, an 8-Sv increase compared to the control run.

6. Altering the southern sinking

We then weakened the SH cell, removing the imposed surface temperature gradient in the Southern Ocean by setting the relaxation temperature to a constant value south of Africa (Fig. 10, bottom panel). This changes the circulation dramatically.

For one, the surface flow in the Southern Ocean is now westward. Instead of having 104 Sv of Drake Passage transport, there is now −11 Sv. As such, the flow over the entire region south of Australia is westward, as opposed to in the control run, where it was westward only in the blocked latitudes. The Agulhas and East Australian Currents feed this flow, yielding a strong flow impinging on the east coast of South America. This feeds the surface WBC in the Atlantic, which is stronger than in the control run and northward over the entire basin.

That current is also deeper, as seen in the section at 1000 m (Fig. 11, upper right), and the NADW is stronger, as seen at 3300 m (Fig. 11, lower right). Notice, too, that the NADW splits in the South Atlantic, with a portion flowing along the eastern side of the mid-Atlantic ridge. Such a partitioning of the NADW has been seen before in both observations and simulations (Hogg 1983; Zangenberg and Siedler 1998; Hogg and Thurnherr 2005; van Sebille et al. 2012). Both branches exit the Atlantic and proceed eastward along ridges in

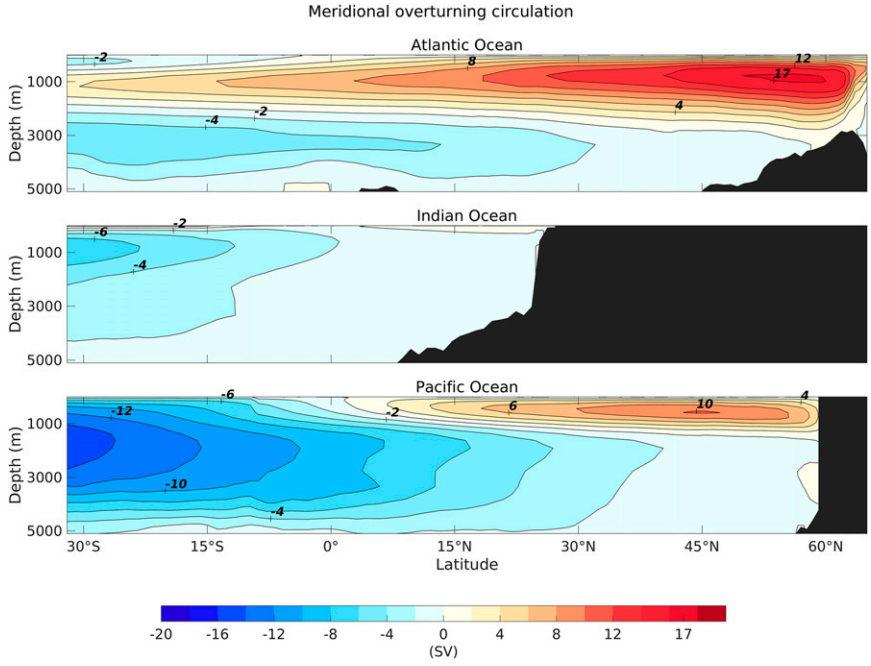

FIG. 7. The meridional overturning streamfunction for the (top) Atlantic Ocean, (middle) Indian Ocean, and (bottom) Pacific Ocean. Positive (negative) values indicates clockwise (anticlockwise) rotation. The Atlantic positive overturning cell spans the entire basin, while it is confined to the northern basin in the Pacific. All three oceans exhibit a deep negative overturning cell, which is the AABW cell.

the Southern Ocean. The flow continues into the Indian and Pacific basins, again on the eastern sides of bathymetric features (the Tonga–Kermadec Arc in the South Pacific and off Madagascar in the Indian). Thus, the NADW is the primary source of abyssal water in the Indian and Pacific basins, in contrast with the control run when the AABW was dominant.

The overturning has also strengthened in the North Pacific. Now the downwelling is strong enough that the WBC at 1000 m flows across the equator. It continues south of Australia and joins the westward flow in the Southern Ocean. The Pacific WBC also extends much deeper (2800 m) than in the control run.

There are large differences in the vertical velocities as well, especially at high latitudes (Fig. 12). The North Atlantic downwelling has more than doubled (37 Sv at 900 m), with the largest increase occurring southeast of Iceland. The upwelling in the WBC has also increased. The result is that the NADW cell more than doubles in strength (40 Sv) and spans the entire depth of the Atlantic basin (Fig. 8, lower right). The downwelling in the North Pacific has also more than doubled (22 Sv). The vertical velocities in the Southern Ocean, on the other hand, are much weaker and are usually associated with isolated bathymetry. But crucially, the interior upwelling is roughly the same at low latitudes (30°S to 30°N) as in the control run.

7. Assessing the vertical motion and the overturning

a. *Dynamical balances*

Three types of vertical motion occur in the model: upwelling in the basin interiors, upwelling and downwelling in lateral boundary layers, and localized vertical motion in regions of strong flow curvature.

In the interior, the buoyancy equation is very nearly in a vertical advective–diffusive balance:

$$w\frac{\partial b}{\partial z} \simeq \kappa_v \frac{\partial^2 b}{\partial z^2}, \tag{1}$$

where w is the vertical velocity and b is the buoyancy. (Recall that the vertical diffusivity κ_v is constant.) Thus, downward diffusion from the surface is balanced by upwelling, as suggested by Munk (1966). The stratification over much of the interior is nearly exponential, that is, $b(z) \propto \exp(\alpha z)$, so that $w \simeq \kappa_v \alpha > 0$ (for some constant alpha). This accounts for the interior upwelling seen in Figs. 9 and 12.

Near the boundaries, lateral mixing dominates vertical mixing. Buoyancy advection by the horizontal velocities is also important, but often approximately cancels:

$$u\frac{\partial b}{\partial x} + v\frac{\partial b}{\partial y} \approx 0.$$

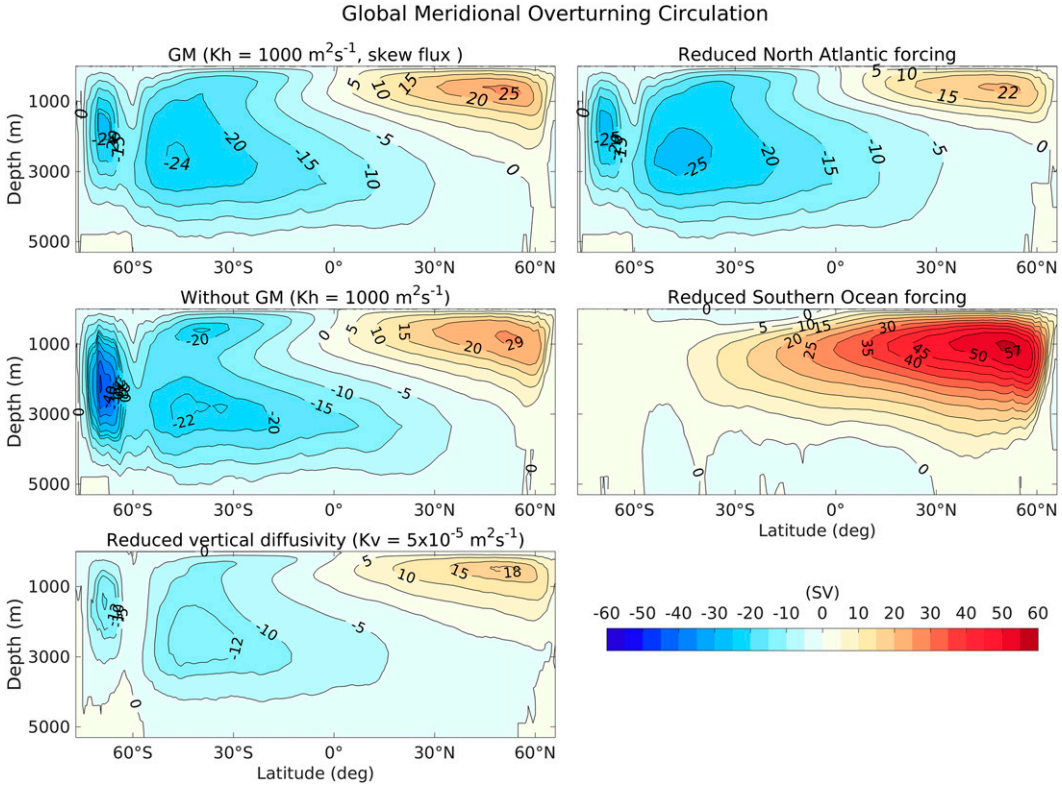

FIG. 8. The global meridional overturning streamfunction for (top left) the control run, (middle left) without the GM parameterization, (bottom left) with reduced vertical diffusivity, (top right) with reduced North Atlantic forcing, and (middle right) with reduced Southern Ocean forcing. Positive (negative) values indicate clockwise (anticlockwise) rotation.

Thus, vertical advection balances lateral mixing:

$$w\frac{\partial b}{\partial z} \simeq \frac{\partial}{\partial \eta}\left(\kappa_h \frac{\partial b}{\partial \eta}\right), \tag{2}$$

if η is the coordinate normal to the boundary and κ_h is the horizontal diffusivity. As such, the vertical velocity depends on the lateral shear, as the tangential velocity is nearly in thermal wind balance with the normal buoyancy gradient:

$$w\frac{\partial b}{\partial z} = f\frac{\partial}{\partial \eta}\left[\kappa_h \frac{\partial}{\partial z}(\hat{\boldsymbol{\eta}} \times \mathbf{u}) \cdot \hat{\mathbf{k}}\right], \tag{3}$$

where f is the Coriolis parameter and u is the horizontal velocity. So, for example, next to the western boundary,

$$w\frac{\partial b}{\partial z} = f\frac{\partial}{\partial x}\left(\kappa_h \frac{\partial v}{\partial z}\right). \tag{4}$$

Both the vertical shear v_z of the meridional velocity and the buoyancy gradient b_z are positive in the NH WBCs. Thus, w has the same sign as v_x (GL17). There is upwelling adjacent to the wall, due to the no-slip condition on the wall, and downwelling offshore (see Fig. 9). The same argument explains the boundary upwelling and sinking in the South Atlantic and also adjacent to the Antarctic coast. In the latter case, $w \propto -fu_{yz}$. Thus, w is positive where the shear is positive—for example, in the region from 0° to 135°E—and negative where the shear is negative, as in the eastern portions of the Ross and Weddell Gyres. Note the horizontal flow reverses in the latter (Fig. 4, middle panel), consistent with the change in sign of w.

Thus, in both the interior and the lateral boundary layers, vertical buoyancy advection is balanced by mixing. This suggests w can be estimated by dividing the total mixing by the buoyancy gradient, as plotted in Fig. 13. The resulting field compares well to the actual one (Fig. 9). The interior upwelling is nearly the same, particularly at low latitudes, and the upwelling in the western boundary layers and near Antarctica is captured. Where the mixing-based estimate is less successful is in the sinking regions in the North Atlantic and North Pacific and in the Ross and Weddell Seas. This is because the stratification in these regions is weak because of convection. Nevertheless, mixing determines the vertical velocity over much of the domain in the model.

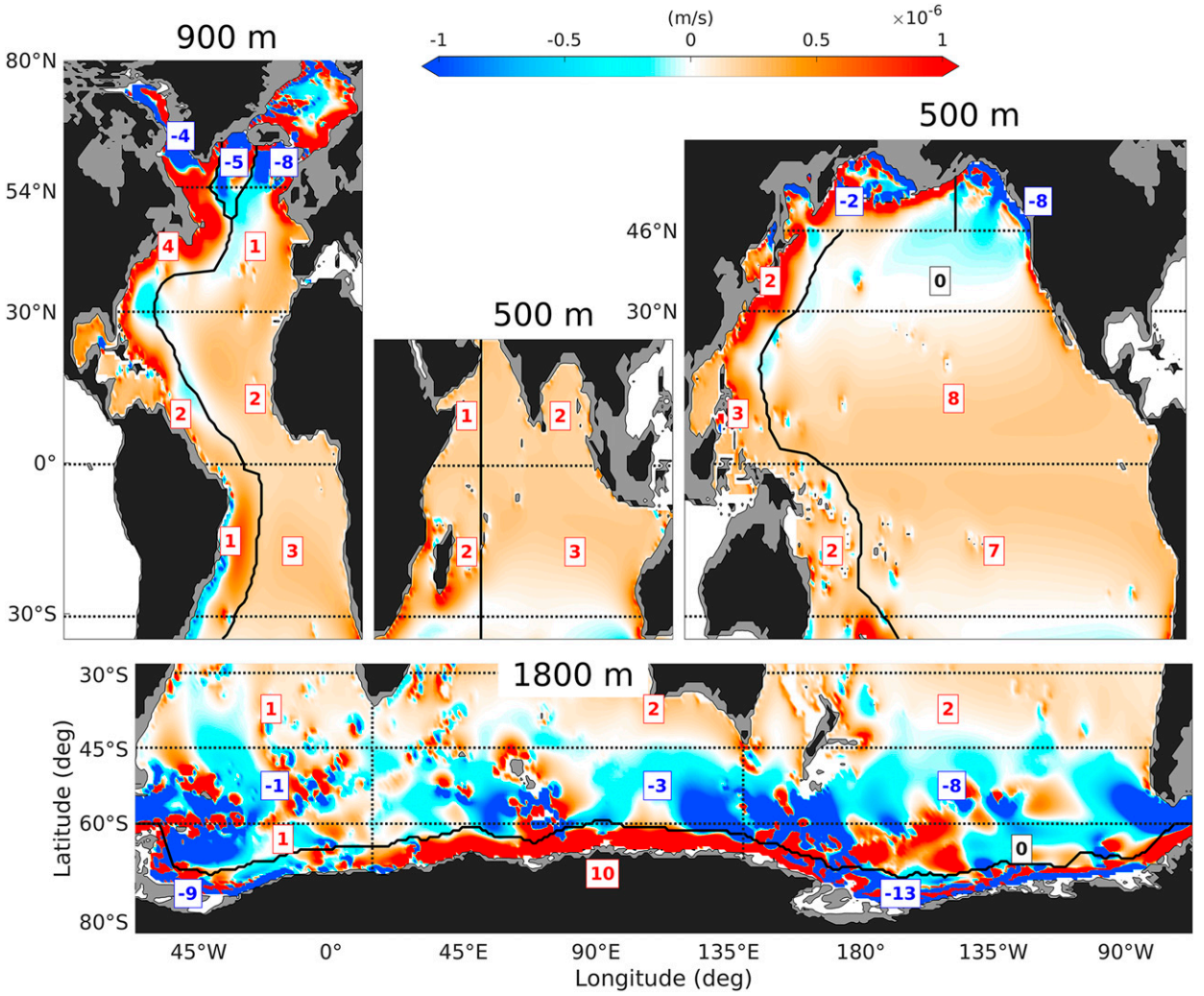

FIG. 9. The vertical velocity for the (top left) Atlantic Ocean at 900-m, (top middle) Indian Ocean at 500-m, (top right) Pacific Ocean at 500-m, and (bottom) Southern Ocean at 1800-m depth. The red (blue) colors indicate positive (negative) vertical velocity. The transports for the different regions are indicated by boxes. All transports are given in Sv.

The mixing-based estimate also misses the localized upwelling and downwelling in the interior Southern Ocean. Here, the vertical motion derives from meridional motion of the ACC. Integrating the Sverdrup relation yields

$$\int_z^0 v(z)\,dz = \frac{f}{\beta}[w(0) - w(z)] = -\frac{f}{\beta}w(z), \qquad (5)$$

where $\beta = df/dy$. Thus, a depth-integrated southward flow implies sinking ($f < 0$) and northward flow upwelling. In many regions, a dipole pattern of upwelling and downwelling is associated with a meander around a topographic feature (e.g., south of New Zealand).

b. *Rationalizing the overturning cells*

There are two primary regions for upwelling in the simulations. The upwelling in the interior is roughly the same in all experiments. The transport is greatest in the wide basins because of the increased area, and as such, the Pacific is the principal interior upwelling site. In addition, upwelling occurs in the WBCs, and the transport is proportional to the lateral shear, as noted. In the Atlantic, the WBC upwelling is roughly equal to that in the basin interior, while in the Pacific, the interior upwelling is greater.

The downwelling, on the other hand, occurs primarily in shear zones near boundaries. In regions where continents block the latitude lines, this happens when thermally driven flow impacts eastern boundaries. The extent of downwelling depends, in turn, on the latitude of the

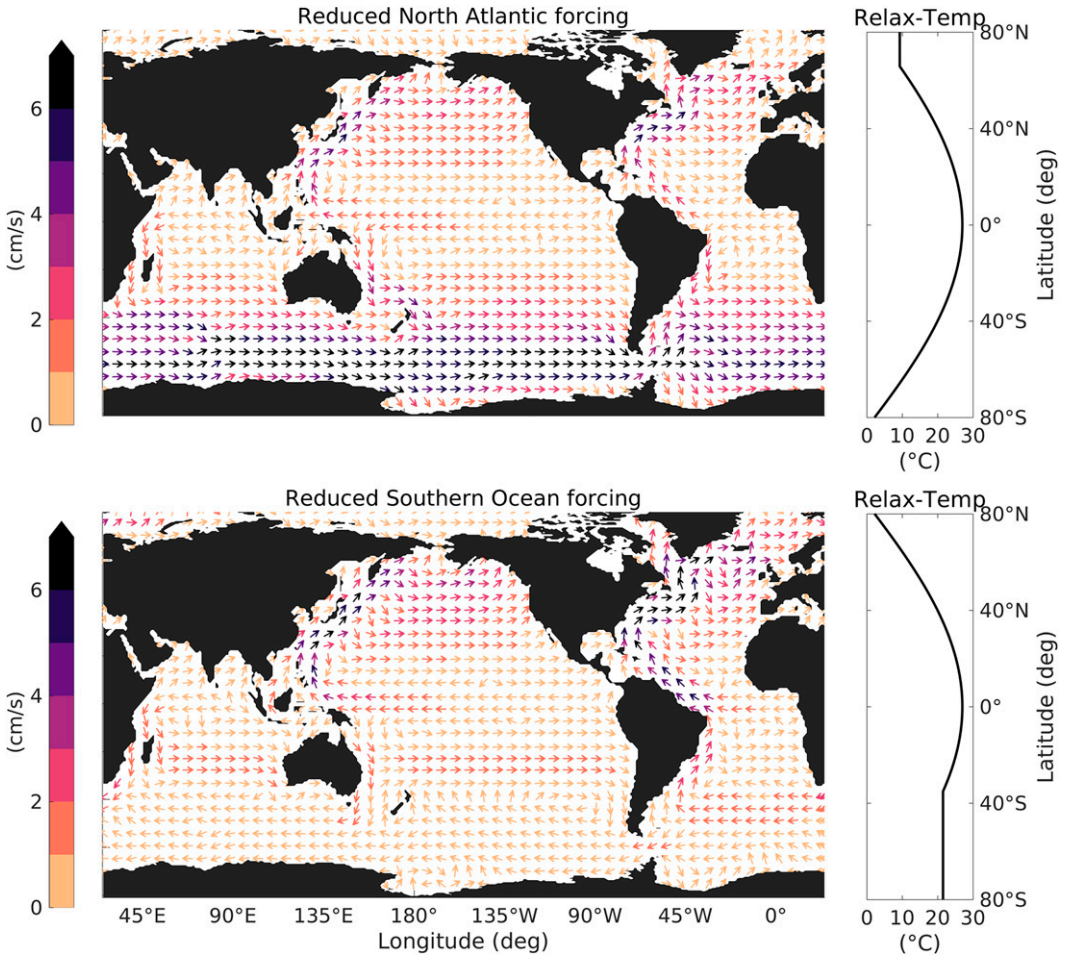

FIG. 10. (left) Surface velocity for reduced forcing in the (top) North Atlantic and (bottom) reduced forcing over the Southern Ocean. The arrows indicate the direction and the colors indicate the strength of the flow. (right) Relaxation temperature profiles for the two simulations.

sinking region. The farther north it is, the more homogeneous the water column, because of convection, and the greater the thermal wind transport associated with the surface forcing (GL17). Second, the ocean depth at the boundary affects how deep the overturning will be. The North Atlantic overturning extends to 2500-m depth, the depth of the sinking region. The latitude of the northern boundary also determines the temperature of the downwelled water. The North Pacific boundary lies to the south of that in the North Atlantic, so the downwelled water is warmer and reaches a shallower level.

In the Southern Ocean, the downwelling occurs primarily in the sheared boundary layers near Antarctica. The deepest waters are produced in the Weddell and Ross Gyres, precisely where the middepth flow is westward and downwelling is favorable, as explained above. Because of its low temperature, the resulting AABW is the densest in the ocean. There is additional downwelling in the interior ACC, due to meridional motion, but this is shallower and often compensated locally by upwelling.

Eliminating the surface temperature gradient in the Nordic Seas reduces the flow impacting the eastern boundary and, hence, the sinking there. More sinking is required in the Southern Ocean to balance the interior upwelling, and this demands a stronger eastward flow to increase the lateral shear near the continent. Hence, the ACC strengthens.

Eliminating the surface temperature gradient in the Southern Ocean, on the other hand, forces the sinking to occur in the northern regions, both in the North Atlantic and North Pacific. This results in stronger WBCs with an associated increase in western boundary upwelling. As such, the northern cells must increase even more to compensate. As such, reducing Southern Ocean sinking has a proportionally greater effect on the overturning cells.

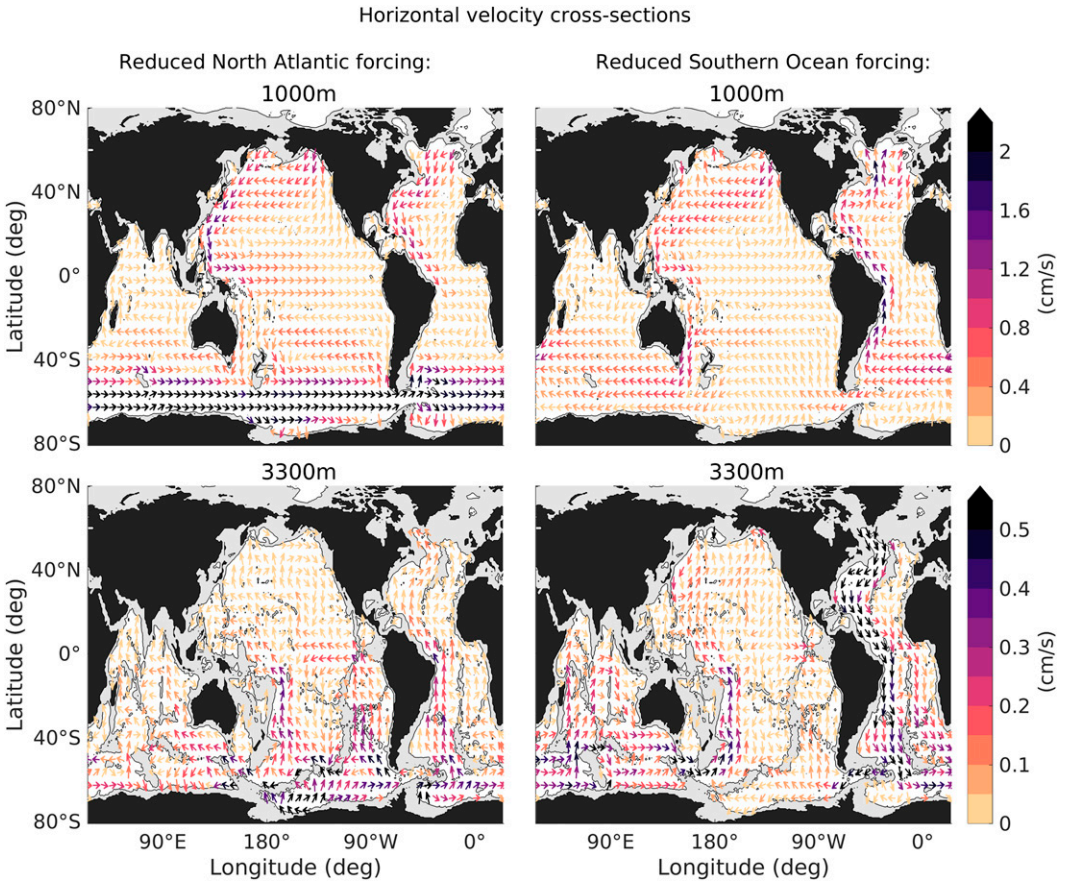

FIG. 11. Horizontal velocity at (top) 1000 and (bottom) 3300 m for reduced forcing in (left) the North Atlantic and (right) reduced forcing over the Southern Ocean. The arrows indicate the direction, and the colors indicate the strength of the flow. Note that the color bars differ for the top and bottom rows. (left column) When the NADW cell is reduced, the flow is similar to that in the control run, but weaker and shallower.

In summary, the overturning is ''pulled'' by interior upwelling in these simulations. The runs differ in where the compensating downwelling occurs, but in all cases, the sinking happens in sheared boundary layers and is related to lateral mixing. Note that the boundary layers in the model are essentially Munk layers (GL17) because of the fairly large horizontal viscosity. However, this is probably unrealistic for the actual ocean, where downwelling often occurs in deepened mixed layers, following the isobaths (Clarke and Gascard 1983; Marshall and Schott 1999).

c. *Impact of the vertical diffusivity*

The present simulations employed a vertical diffusivity, $\kappa_v = 10^{-4}\,\mathrm{m^2\,s^{-1}}$, which is comparable to the estimated global mean value (e.g., Munk 1966; Munk and Wunsch 1998; Lumpkin and Speer 2007; Waterhouse et al. 2014). This is, however, roughly an order of magnitude larger than diffusivities observed over much of the ocean interior (Lumpkin and Speer 2007). To gauge the effect of having a weaker diffusivity, we conducted an additional run, with $\kappa_v = 5 \times 10^{-5}\,\mathrm{m^2\,s^{-1}}$ and increased vertical resolution (34 layers).

In general, the overturning and the horizontal and vertical velocities are qualitatively consistent with those in the control run (not shown). However, as seen in the lower-left panel of Fig. 8, the overturning cells are weaker. The maximum overturning in the North Atlantic is reduced by roughly 25%, from 20 to 15 Sv, and the AABW cell is weakened even more, by roughly 40%. This is consistent with having weaker upwelling in the interior driving the global circulation.

Traditional scaling (e.g., Robinson and Stommel 1959; Colin de Verdière 1988; Vallis 2006) suggests that the overturning should vary as $\kappa_v^{2/3}$. A number of idealized studies conducted with this model, including GL17, found a weaker dependence of $\kappa_v^{2/5}$ (see also Park and Bryan 2000). The 25% decrease in the NADW overturning here is consistent with the $\kappa_v^{2/5}$ dependence.

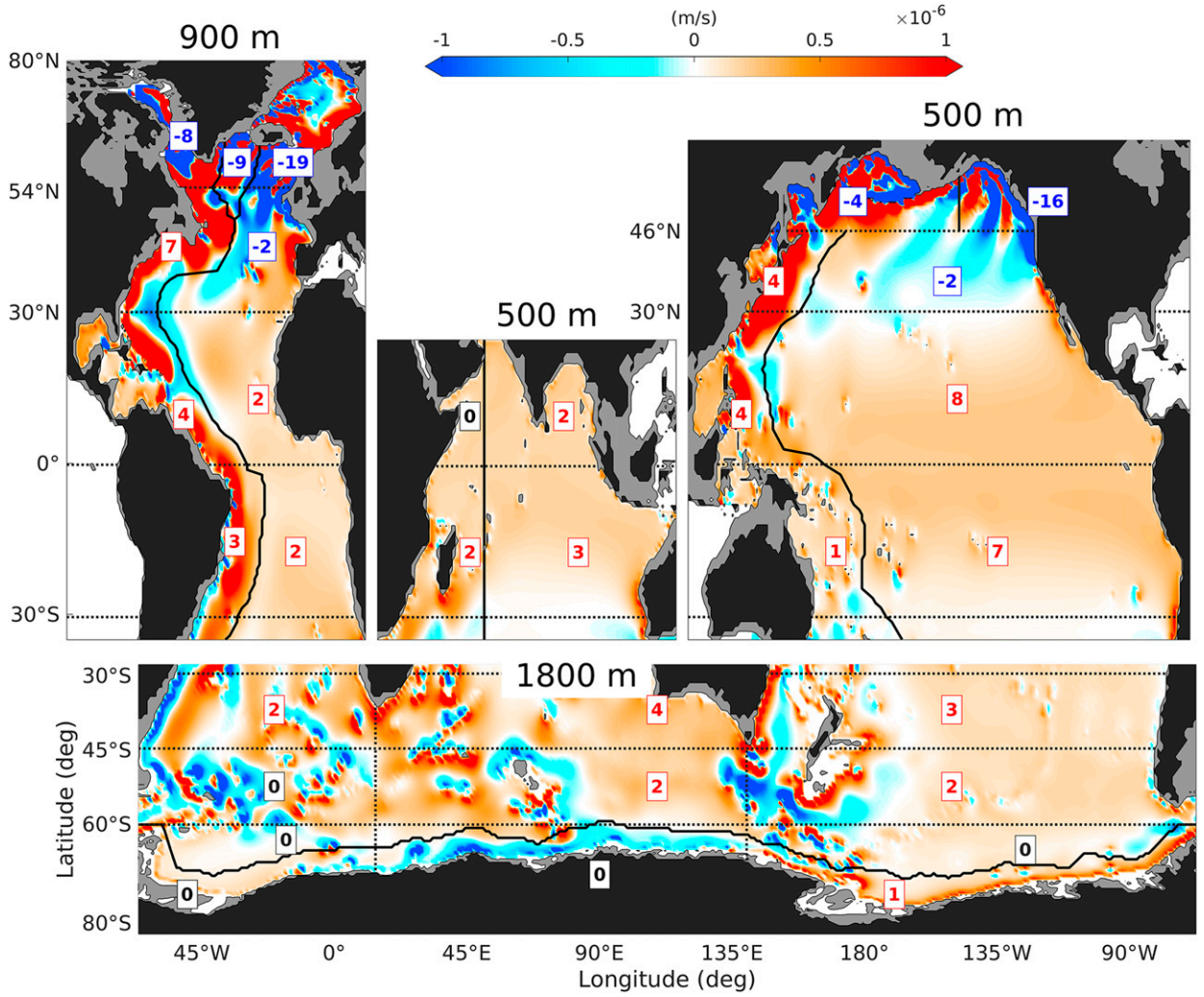

FIG. 12. The vertical velocity for reduced Southern Ocean forcing simulation for the (top left) Atlantic Ocean at 900-m, (top middle) Indian Ocean at 500-m, (top right) Pacific Ocean at 500-m, and (bottom) Southern Ocean at 1800-m depth. The red (blue) colors indicate positive (negative) vertical velocity. The transports for the different regions are indicated by boxes. All transports are given in Sv.

However, the decrease in the AABW cell is greater than expected. This likely reflects more complex dynamics in the abyss and the Southern Ocean than envisioned in the scaling. Similar dependencies with GCMs were observed recently by M. Nikurashin (2017, personal communication).

Our use of a constant diffusivity is fairly typical in ocean-only studies (e.g., Abernathey et al. 2011; Marshall et al. 2014, 2015; Armour et al. 2016). In reality, the vertical diffusivity varies greatly with depth and location (e.g., Waterhouse et al. 2014), being intensified near the surface over rough bathymetry (Polzin et al. 1997; Ledwell et al. 2000) and near continental boundaries (e.g., Ledwell and Hickey 1995). Spatially variable diffusivities can produce additional upwelling and downwelling, and this can affect, for example, the AABW, being the dominant cell in the abyss (Simmons et al. 2004; Saenko and Merryfield 2005; Mashayek et al. 2015; Ferrari et al. 2016; McDougall and Ferrari 2017). In the present context, we would expect less upwelling in the interior and more in the WBCs so that the latter could well dominate upwelling in the actual ocean. That could complicate global upwelling estimates, since WBC upwelling depends on the lateral shear, which in turn depends on the strength of the overturning. Further, the Pacific would not necessarily be the dominant location for upwelling but would contribute like the other basins via its western boundary currents. Our understanding of the effects of variable diffusivities is developing, and future studies will elucidate the modifications in thermally driven flows like this.

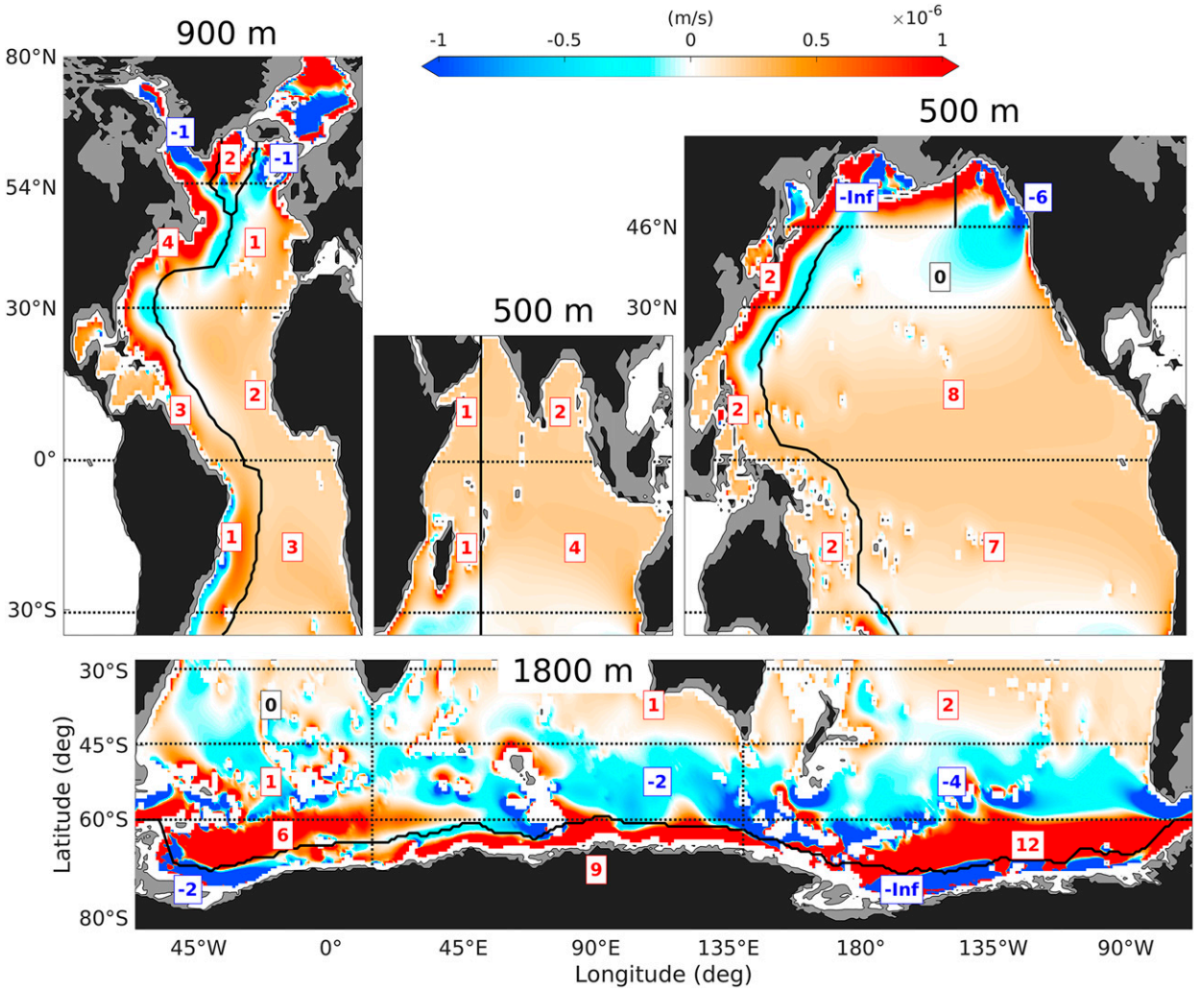

FIG. 13. The vertical velocity estimated by the ratio of the total mixing and the vertical buoyancy gradient for the (top left) Atlantic Ocean at 900-m, (top middle) Indian Ocean at 500-m, (top right) Pacific Ocean at 500-m, and (bottom) Southern Ocean at 1800-m depth. The red (blue) colors indicate positive (negative) vertical velocity. The transports for the different regions are indicated by boxes. All transports are given in Sv.

d. Impact of the GM scheme

As noted, the simulations were performed with the Gent and Mcwilliams parameterization for lateral mixing. Running the model without the GM scheme, using a constant horizontal diffusivity of $1000\,m^2\,s^{-1}$, yields the overturning circulation shown in the middle left panel of Fig. 8. The primary difference from the control run (upper-left panel) is that the overturning near Antarctica is nearly twice as strong. Thus, the Veronis effect (Veronis 1975) enhances both the sinking and upwelling in the lateral shear zones (as the isotherms are nearly vertical there). However, over much of the rest of the domain, the changes are smaller. In particular, AABW and NADW production are largely unchanged.

8. Summary and conclusions

We have examined the global ocean circulation with realistic bathymetry, driven solely by surface temperature forcing. Explicit wind forcing is excluded, although vertical mixing is retained. The character of the resulting flow is consistent in many ways with the observed ocean circulation, with baroclinic WBCs, a strong ACC in the Southern Ocean, and an overturning circulation that closely resembles those obtained in full GCMs and in observations. However, we emphasize that the strength of the overturning is strongly dependent on the vertical diffusivity, assumed to be constant here.

The vertical velocity is a critical element in understanding the large-scale circulation. The overturning is

primarily driven by diffusively driven upwelling in the basin interiors. In the control run, the downwelling is equally distributed between the Northern and Southern Hemispheres and occurs in frictional boundary layers. That sinking depends on the horizontal shear, which is driven by the imposed surface temperature gradient. Eliminating the surface gradient in either hemisphere requires stronger horizontal flow in the other hemisphere to increase the downwelling there. Thus, reducing the sinking in the Nordic Seas results in a stronger ACC, with greater sinking in the Weddell and Ross Seas. Eliminating the (thermally forced) ACC, on the other hand, increases the production of NADW and North Pacific Deep Water as well. The connections between the various overturning cells have been explored previously (e.g., Cox 1989; England 1993; Goodman 1998; Kamenkovich and Goodman 2000; Kamenkovich and Radko 2011), as has their tendency to compensate one another (Stocker and Johnsen 2003). But as these studies employed wind and salinity forcing, the connections were harder to distinguish.

There are two different water paths that feed the Atlantic WBC. That involving westward flow through Drake Passage and continuing along South America is known as the cold route (Rintoul 1991). The warm route (Gordon 1986) involves return flow from the Indian–Pacific sector via the Agulhas Current to the Atlantic. There has been much discussion on the relative importance of these routes for the overturning (e.g., Speich et al. 2001, 2002; Talley et al. 2003; Lumpkin and Speer 2007). The present simulations suggest the warm route is favored in the absence of direct forcing in the Southern Ocean. This is in line with theory because westward flows are preferred on the β plane without forcing (Bretherton and Haidvogel 1976). With forcing (either by surface thermal forcing or winds), the Southern Ocean flow can instead be eastward, favoring the cold route.

We have neglected wind forcing, evaporation/precipitation, and ice cover, all of which will modify the surface forcing. Wind forcing will impact the direction of the WBCs and also the character of the interior flow (Hecht and Smith 2013). Instead of broad eastward zonal flow, the interior velocities will be focused between subtropical and subpolar gyres, and the WBC will separate from the western boundary between them. This will prevent the WBC penetrating to high latitudes, as happens here. Wind forcing will also increase the heat transport at shallower levels, as warm water is advected north by the Gulf Stream (Ferrari and Ferreira 2011; Talley et al. 2003) and will generate northward Ekman transport in the Southern Ocean, yielding upwelling of Antarctic Intermediate Water (Marshall and Speer 2012; Nikurashin and Vallis 2012). Saenko et al. (2002) found that excluding winds yielded a slightly reduced overturning in the Atlantic and a much weaker NADW outflow, though the large-scale overturning was very similar.

The overturning in the North Pacific in our simulations was half as large as that in the North Atlantic. In reality, the production of North Pacific Deep Water is believed to be much less than that of NADW. This has been attributed to excess freshwater input from precipitation (Ferreira et al. 2010; Saenko et al. 2002). It is also possible that wind forcing alters sinking along the eastern boundary but redirects the flow in the gyres. Ice at high latitudes also modifies surface forcing. Saenko (2009) and Timmermann and Goosse (2004) observed a collapse in the Atlantic MOC when removing the winds, and this was likely due to the ice edge expanding equatorward, shielding the ocean from surface forcing. This varies between models, though. Saenko et al. (2002) found only a 20% reduction in the Atlantic MOC without winds. The position of the ice edge is linked to ocean heat transport (Winton 2003) and so should respond to the thermally driven circulation.

If the present results can be extrapolated to the ocean, changes in surface forcing will alter the MOCs. Polar amplification in particular will reduce the meridional temperature gradient (Serreze and Francis 2006; Screen and Simmonds 2010), and this should weaken the overturning. We are currently investigating to what extent this happens in fully coupled climate models.

Acknowledgments. We benefited from discussions with Anne Fouilloux and David Ferreira and from constructive comments from two anonymous reviewers. The research was conducted with computational resources at UiO provided by NORTUR (http:///www.sigma2.no). JHL was supported in part by Grant NORSEE from the Norwegian Research Council.

APPENDIX

The Meridional Overturning in Latitude–Temperature Space

Averaging the transport in density space (instead of depth) is more consistent with the fluid pathways (e.g., Döös and Webb 1994; Nycander et al. 2007; Ferrari and Ferreira 2011; Döös et al. 2012; Zika et al. 2012). Thus, we examine the global overturning streamfunction in density space here for completeness. As density variations are determined solely by temperature here, we calculate the streamfunction in latitude–temperature space (Ferrari and Ferreira 2011):

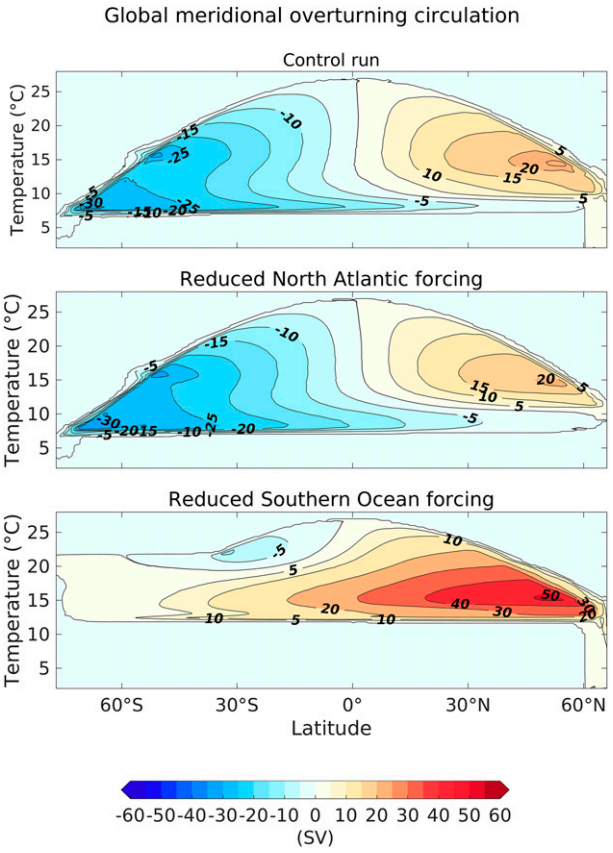

FIG. A1. The global meridional overturning streamfunction in latitude–temperature space for the (top) control run, (middle) with reduced North Atlantic forcing, and (bottom) with reduced Southern Ocean forcing. Positive (negative) values indicate clockwise (anticlockwise) rotation.

$$\Psi(y,\theta) = \int\int_{\theta_B}^{\theta} v\,dx\,dz\,, \qquad \text{(A1)}$$

where $\theta(x, y, z)$ is a two-dimensional isothermal surface, and $\theta_B(x, y, -H)$ is the temperature at the bottom of the ocean.

The result for the control run is shown in Fig. A1 (upper panel). As before, two cells are seen: one associated with northern sinking and the other associated with sinking in the Southern Ocean. The streamlines tilt at the warmer temperatures, indicating cross-isothermal transport (diapycnal transformation). This occurs when the poleward surface flows encounter warming (cooling) at low (high) latitudes from the imposed temperature forcing. Below the thermocline, the streamlines are relatively flat, indicating nearly isothermal flow.

The northern cell is the combined North Atlantic and North Pacific overturning and is confined to the NH. The amplitude of 22 Sv is slightly weaker, compared to the latitude–depth overturning (25 Sv in Fig. 8), as the more shallow North Pacific overturning occurs at warmer temperatures, compared to the Atlantic. The coldest waters occur in the southern cell. The two subcells seen in Fig. 8 and discussed in section 4b are present; the colder cell compromises the upwelling and downwelling along the Antarctic continent, while the warmer is associated with downwelling in the northern part of the Southern Ocean and in the Drake Passage (also see Fig. 9). The cross-equatorial transport along the bottom ridges is evident at the coldest temperatures.

The upwelling branches of overturning cells exhibit nearly vertical streamlines as the water mixes with warmer water masses. The undulations at lower latitudes in the AABW cell are due to warmer temperatures in the Indian Ocean branch of the cell, compared to the Pacific branch. This is evident when plotting the overturning by basin (not shown). The latitude–temperature overturning streamfunctions for the additional runs with reduced North Atlantic and Southern Ocean temperature forcing are shown in Fig. A1 (middle and lower panels). When the surface temperature gradient is removed north of 64°N, the global overturning is similar to the control run. However, the Atlantic overturning is reduced, as discussed in section 7, and the production of very cold water north of 60°N is absent. When the gradient is removed south of 34°S, the AABW cell weakens greatly, and the streamlines tilt less (caused by having a constant SST; Fig. A1, lower panel). The abyss is accordingly warmer. The northern cell more than doubles in strength, with the overturning occurring over the same temperatures as in the control run. The cell also extends much farther south, as the upwelling occurs over a larger latitude range, because of the enhanced sinking. The return branch is now tilted as well, as a large fraction of the return flow is at the surface (see Fig. 10) and exposed to surface forcing. The small blue cell in the SH, north of 34°S, is nearly absent in latitude–depth coordinates (see Fig. 8). It reflects the southward WBCs along Africa and Australia and the return flow below.

Thus, the temperature-averaged overturning cells largely confirm those obtained when averaging over depth. As suggested by a reviewer, the streamfunctions seen here can also be plotted versus depth, if one uses the mean depths of the isotherms. This yields cells that are more similar to the depth-averaged ones, albeit confined to shallower depths (not shown).

REFERENCES

Abernathey, R., J. Marshall, and D. Ferreira, 2011: The dependence of Southern Ocean meridional overturning on wind stress. *J. Phys. Oceanogr.*, **41**, 2261–2278, https://doi.org/10.1175/JPO-D-11-023.1.

Amante, C., and B. W. Eakins, 2008: ETOPO1 1 arc-minute global relief model: Procedures, data sources and analysis. NOAA Tech. Memo. NESDIS NGDC-24, 25 pp., https://www.ngdc.noaa.gov/mgg/global/relief/ETOPO1/docs/ETOPO1.pdf.

Armour, K. C., J. Marshall, J. R. Scott, A. Donohoe, and E. R. Newsom, 2016: Southern Ocean warming delayed by circumpolar upwelling and equatorward transport. *Nat. Geosci.*, **9**, 549–554, https://doi.org/10.1038/ngeo2731.

Bretherton, F. P., and D. B. Haidvogel, 1976: Two-dimensional turbulence above topography. *J. Fluid Mech.*, **78**, 129–154, https://doi.org/10.1017/S002211207600236X.

Bryan, F., 1987: Parameter sensitivity of primitive equation ocean general circulation models. *J. Phys. Oceanogr.*, **17**, 970–985, https://doi.org/10.1175/1520-0485(1987)017<0970:PSOPEO>2.0.CO;2.

Cai, W., 1994: Circulation driven by observed surface thermohaline fields in a coarse resolution ocean general circulation model. *J. Geophys. Res.*, **99**, 10 163–10 181, https://doi.org/10.1029/93JC03565.

——, and P. G. Baines, 1996: Interactions between thermohaline- and wind-driven circulations and their relevance to the dynamics of the Antarctic Circumpolar Current, in a coarse-resolution global ocean general circulation model. *J. Geophys. Res.*, **101**, 14 073–14 093, https://doi.org/10.1029/96JC00669.

Clarke, R. A., and J.-C. Gascard, 1983: The formation of Labrador Sea Water. Part I: Large-scale processes. *J. Phys. Oceanogr.*, **13**, 1764–1778, https://doi.org/10.1175/1520-0485(1983)013<1764:TFOLSW>2.0.CO;2.

Colin de Verdière, A., 1988: Buoyancy driven planetary flows. *J. Mar. Res.*, **46**, 215–265, https://doi.org/10.1357/002224088785113667.

Cox, M. D., 1989: An idealized model of the World Ocean. Part I: The global-scale water masses. *J. Phys. Oceanogr.*, **19**, 1730–1752, https://doi.org/10.1175/1520-0485(1989)019<1730:AIMOTW>2.0.CO;2.

Cunningham, S., S. Alderson, B. King, and M. Brandon, 2003: Transport and variability of the Antarctic Circumpolar Current in Drake Passage. *J. Geophys. Res.*, **108**, 8084, https://doi.org/10.1029/2001JC001147.

Donohue, K. A., K. L. Tracey, D. R. Watts, M. P. Chidichimo, and T. K. Chereskin, 2016: Mean Antarctic Circumpolar Current transport measured in Drake Passage. *Geophys. Res. Lett.*, **43**, 11 760–11 767, https://doi.org/10.1002/2016GL070319.

Döös, K., and D. J. Webb, 1994: The Deacon cell and the other meridional cells of the Southern Ocean. *J. Phys. Oceanogr.*, **24**, 429–442, https://doi.org/10.1175/1520-0485(1994)024<0429:TDCATO>2.0.CO;2.

——, J. Nilsson, J. Nycander, L. Brodeau, and M. Ballarotta, 2012: The World Ocean thermohaline circulation. *J. Phys. Oceanogr.*, **42**, 1445–1460, https://doi.org/10.1175/JPO-D-11-0163.1.

England, M. H., 1993: Representing the global-scale water masses in ocean general circulation models. *J. Phys. Oceanogr.*, **23**, 1523–1552, https://doi.org/10.1175/1520-0485(1993)023<1523:RTGSWM>2.0.CO;2.

Ferrari, R., and D. Ferreira, 2011: What processes drive the ocean heat transport? *Ocean Modell.*, **38**, 171–186, https://doi.org/10.1016/j.ocemod.2011.02.013.

——, A. Mashayek, T. J. McDougall, M. Nikurashin, and J.-M. Campin, 2016: Turning ocean mixing upside down. *J. Phys. Oceanogr.*, **46**, 2239–2261, https://doi.org/10.1175/JPO-D-15-0244.1.

Ferreira, D., J. Marshall, and J.-M. Campin, 2010: Localization of deep water formation: Role of atmospheric moisture transport and geometrical constraints on ocean circulation. *J. Climate*, **23**, 1456–1476, https://doi.org/10.1175/2009JCLI3197.1.

Gent, P. R., and J. C. Mcwilliams, 1990: Isopycnal mixing in ocean circulation models. *J. Phys. Oceanogr.*, **20**, 150–155, https://doi.org/10.1175/1520-0485(1990)020<0150:IMIOCM>2.0.CO;2.

Gill, A., and K. Bryan, 1971: Effects of geometry on the circulation of a three-dimensional Southern-Hemisphere ocean model. *Deep-Sea Res. Oceanogr. Abstr.*, **18**, 685–721, https://doi.org/10.1016/0011-7471(71)90086-6.

Gjermundsen, A. and J. H. LaCasce, 2017: Comparing the linear and nonlinear buoyancy-driven circulation. *Tellus*, **69A**, 1299282, https://doi.org/10.1080/16000870.2017.1299282.

Gnanadesikan, A., and R. W. Hallberg, 2000: On the relationship of the circumpolar current to Southern Hemisphere winds in coarse-resolution ocean models. *J. Phys. Oceanogr.*, **30**, 2013–2034, https://doi.org/10.1175/1520-0485(2000)030<2013:OTROTC>2.0.CO;2.

Goodman, P. J., 1998: The role of North Atlantic Deep Water formation in an OGCM's ventilation and thermohaline circulation. *J. Phys. Oceanogr.*, **28**, 1759–1785, https://doi.org/10.1175/1520-0485(1998)028<1759:TRONAD>2.0.CO;2.

Gordon, A. L., 1986: Interocean exchange of thermocline water. *J. Geophys. Res.*, **91**, 5037–5046, https://doi.org/10.1029/JC091iC04p05037.

Hecht, M. W., and R. D. Smith, 2013: Toward a physical understanding of the North Atlantic: A review of model studies in an eddying regime. *Ocean Modeling in an Eddying Regime*, M. W. Hecht and H. Hasumi, Eds., Amer. Geophys. Union, 213–239, https://doi.org/10.1029/177GM15.

Hogg, N. G., 1983: A note on the deep circulation of the western North Atlantic: Its nature and causes. *Deep-Sea Res.*, **30**, 945–961, https://doi.org/10.1016/0198-0149(83)90050-X.

——, and A. M. Thurnherr, 2005: A zonal pathway for NADW in the South Atlantic. *J. Oceanogr.*, **61**, 493–507, https://doi.org/10.1007/s10872-005-0058-7.

Hua, B., D. Moore, and S. Le Gentil, 1997: Inertial nonlinear equilibration of equatorial flows. *J. Fluid Mech.*, **331**, 345–371, https://doi.org/10.1017/S0022112096004016.

Huck, T., and G. K. Vallis, 2001: Linear stability analysis of the three-dimensional thermally-driven ocean circulation: Application to interdecadal oscillations. *Tellus*, **53**, 526–545, https://doi.org/10.3402/tellusa.v53i4.12225.

——, A. J. Weaver, and A. Colin de Verdière, 1999: On the influence of the parameterization of lateral boundary layers on the thermohaline circulation in coarse-resolution ocean models. *J. Mar. Res.*, **57**, 387–426, https://doi.org/10.1357/002224099764805138.

Hughes, G. O., A. M. C. Hogg, and R. W. Griffiths, 2009: Available potential energy and irreversible mixing in the meridional overturning circulation. *J. Phys. Oceanogr.*, **39**, 3130–3146, https://doi.org/10.1175/2009JPO4162.1.

Kamenkovich, I. V., and P. J. Goodman, 2000: The dependence of AABW transport in the Atlantic on vertical diffusivity. *Geophys. Res. Lett.*, **27**, 3739–3742, https://doi.org/10.1029/2000GL011675.

——, and T. Radko, 2011: Role of the Southern Ocean in setting the Atlantic stratification and meridional overturning circulation. *J. Mar. Res.*, **69**, 277–308, https://doi.org/10.1357/002224011798765286.

Klinger, B. A., J. Marshall, and U. Send, 1996: Representation of convective plumes by vertical adjustment. *J. Geophys. Res.*, **101**, 18 175–18 182, https://doi.org/10.1029/96JC00861.

LaCasce, J., 2004: Diffusivity and viscosity dependence in the linear thermocline. *J. Mar. Res.*, **62**, 743–769, https://doi.org/10.1357/0022240042880864.

Ledwell, J. R., and B. M. Hickey, 1995: Evidence for enhanced boundary mixing in the Santa Monica Basin. *J. Geophys. Res.*, **100**, 20 665–20 679, https://doi.org/10.1029/94JC01182.

——, E. T. Montgomery, K. L. Polzin, L. St. Laurent, R. W. Schmitt, and J. M. Toole, 2000: Evidence for enhanced mixing over rough topography in the abyssal ocean. *Nature*, **403**, 179–182, https://doi.org/10.1038/35003164.

Locarnini, R. A., and Coauthors, 2013: *Temperature.* Vol. 1, *World Ocean Atlas 2013*, NOAA Atlas NESDIS 73, 40 pp.

Lumpkin, R., and K. Speer, 2007: Global ocean meridional overturning. *J. Phys. Oceanogr.*, **37**, 2550–2562, https://doi.org/10.1175/JPO3130.1.

Marotzke, J., 1997: Boundary mixing and the dynamics of three-dimensional thermohaline circulations. *J. Phys. Oceanogr.*, **27**, 1713–1728, https://doi.org/10.1175/1520-0485(1997)027<1713:BMATDO>2.0.CO;2.

——, and J. R. Scott, 1999: Convective mixing and the thermohaline circulation. *J. Phys. Oceanogr.*, **29**, 2962–2970, https://doi.org/10.1175/1520-0485(1999)029<2962:CMATTC>2.0.CO;2.

Marshall, J., and F. Schott, 1999: Open-ocean convection: Observations, theory, and models. *Rev. Geophys.*, **37**, 1–64, https://doi.org/10.1029/98RG02739.

——, and R. A. Plumb, 2007: *Atmosphere, Ocean and Climate Dynamics: An Introductory Text.* Academic Press, 344 pp.

——, and K. Speer, 2012: Closure of the meridional overturning circulation through Southern Ocean upwelling. *Nat. Geosci.*, **5**, 171–180, https://doi.org/10.1038/ngeo1391.

——, A. Adcroft, C. Hill, L. Perelman, and C. Heisey, 1997a: A finite-volume, incompressible Navier Stokes model for studies of the ocean on parallel computers. *J. Geophys. Res.*, **102**, 5753–5766, https://doi.org/10.1029/96JC02775.

——, C. Hill, L. Perelman, and A. Adcroft, 1997b: Hydrostatic, quasi-hydrostatic, and nonhydrostatic ocean modeling. *J. Geophys. Res.*, **102**, 5733–5752, https://doi.org/10.1029/96JC02776.

——, K. C. Armour, J. R. Scott, Y. Kostov, U. Hausmann, D. Ferreira, T. G. Shepherd, and C. M. Bitz, 2014: The ocean's role in polar climate change: Asymmetric Arctic and Antarctic responses to greenhouse gas and ozone forcing. *Philos. Trans. Roy. Soc. London*, **A372**, 20130040, https://doi.org/10.1098/rsta.2013.0040.

——, J. Scott, K. Armour, J. Campin, M. Kelley, and A. Romanou, 2015: The ocean's role in the transient response of climate to abrupt greenhouse gas forcing. *Climate Dyn.*, **44**, 2287–2299, https://doi.org/10.1007/s00382-014-2308-0.

Mashayek, A., R. Ferrari, M. Nikurashin, and W. R. Peltier, 2015: Influence of enhanced abyssal diapycnal mixing on stratification and the ocean overturning circulation. *J. Phys. Oceanogr.*, **45**, 2580–2597, https://doi.org/10.1175/JPO-D-15-0039.1.

McDougall, T. J., and R. Ferrari, 2017: Abyssal upwelling and downwelling driven by near-boundary mixing. *J. Phys. Oceanogr.*, **47**, 261–283, https://doi.org/10.1175/JPO-D-16-0082.1.

Ménesguen, C., B. L. Hua, M. Fruman, and R. Schopp, 2009: Dynamics of the combined extra-equatorial and equatorial deep jets in the Atlantic. *J. Mar. Res.*, **67**, 323–346, https://doi.org/10.1357/002224009789954766.

Meredith, M. P., and Coauthors, 2011: Sustained monitoring of the Southern Ocean at Drake Passage: Past achievements and future priorities. *Rev. Geophys.*, **49**, RG4005, https://doi.org/10.1029/2010RG000348.

Munk, W. H., 1966: Abyssal recipes. *Deep-Sea Res. Oceanogr. Abstr.*, **13**, 707–730, https://doi.org/10.1016/0011-7471(66)90602-4.

——, and C. Wunsch, 1998: Abyssal recipes II: Energetics of tidal and wind mixing. *Deep-Sea Res. I*, **45**, 1977–2010, https://doi.org/10.1016/S0967-0637(98)00070-3.

Nikurashin, M., and G. Vallis, 2012: A theory of the interhemispheric meridional overturning circulation and associated stratification. *J. Phys. Oceanogr.*, **42**, 1652–1667, https://doi.org/10.1175/JPO-D-11-0189.1.

Nycander, J., J. Nilsson, K. Döös, and G. Broström, 2007: Thermodynamic analysis of ocean circulation. *J. Phys. Oceanogr.*, **37**, 2038–2052, https://doi.org/10.1175/JPO3113.1.

Paparella, F., and W. Young, 2002: Horizontal convection is non-turbulent. *J. Fluid Mech.*, **466**, 205–214, https://doi.org/10.1017/S0022112002001313.

Park, Y.-G., 2006: Dependence of an eastern boundary current on the horizontal resolution in thermally driven circulations. *J. Geophys. Res.*, **111**, C09005, https://doi.org/10.1029/2005JC003362.

——, and K. Bryan, 2000: Comparison of thermally driven circulations from a depth-coordinate model and an isopycnal-layer model. Part I: Scaling-law sensitivity to vertical diffusivity. *J. Phys. Oceanogr.*, **30**, 590–605, https://doi.org/10.1175/1520-0485(2000)030<0590:COTDCF>2.0.CO;2.

——, and ——, 2001: Comparison of thermally driven circulations from a depth-coordinate model and an isopycnal-layer model. Part II: The difference and structure of the circulations. *J. Phys. Oceanogr.*, **31**, 2612–2624, https://doi.org/10.1175/1520-0485(2001)031<2612:COTDCF>2.0.CO;2.

Pedlosky, J., 1969: Linear theory of the circulation of a stratified ocean. *J. Fluid Mech.*, **35**, 185–205, https://doi.org/10.1017/S0022112069001030.

——, and M. A. Spall, 2005: Boundary intensification of vertical velocity in a β-plane basin. *J. Phys. Oceanogr.*, **35**, 2487–2500, https://doi.org/10.1175/JPO2832.1.

Picaut, J., and R. Tournier, 1991: Monitoring the 1979–1985 equatorial Pacific current transports with expendable bathythermograph data. *J. Geophys. Res.*, **96**, 3263–3277, https://doi.org/10.1029/90JC02066.

Polzin, K., J. Toole, J. Ledwell, and R. Schmitt, 1997: Spatial variability of turbulent mixing in the abyssal ocean. *Science*, **276**, 93–96, https://doi.org/10.1126/science.276.5309.93.

Rintoul, S. R., 1991: South Atlantic interbasin exchange. *J. Geophys. Res.*, **96**, 2675–2692, https://doi.org/10.1029/90JC02422.

Robinson, A., and H. Stommel, 1959: The oceanic thermocline and the associated thermohaline circulation. *Tellus*, **11**, 295–308, https://doi.org/10.1111/j.2153-3490.1959.tb00035.x.

Saenko, O. A., 2009: On the climatic impact of wind stress. *J. Phys. Oceanogr.*, **39**, 89–106, https://doi.org/10.1175/2008JPO3981.1.

——, and W. Merryfield, 2005: On the effect of topographically enhanced mixing on the global ocean circulation. *J. Phys. Oceanogr.*, **35**, 826–834, https://doi.org/10.1175/JPO2722.1.

——, J. M. Gregory, A. J. Weaver, and M. Eby, 2002: Distinguishing the influence of heat, freshwater, and momentum fluxes on ocean circulation and climate. *J. Climate*, **15**, 3686–3697, https://doi.org/10.1175/1520-0442(2002)015<3686:DTIOHF>2.0.CO;2.

Saenz, J., A. Hogg, G. Hughes, and R. Griffiths, 2012: Mechanical power input from buoyancy and wind to the circulation in an ocean model. *Geophys. Res. Lett.*, **39**, L13605, https://doi.org/10.1029/2012GL052035.

Sandström, J. W., 1908: Dynamische Versuche mit Meerwasser. *Ann. Hydrogr. Marit. Meteor.*, **36**, 6–23.

Schloesser, F., R. Furue, J. P. McCreary Jr., and A. Timmermann, 2012: Dynamics of the Atlantic meridional overturning circulation. Part 1: Buoyancy-forced response. *Prog. Oceanogr.*, **101**, 33–62, https://doi.org/10.1016/j.pocean.2012.01.002.

Screen, J. A., and I. Simmonds, 2010: The central role of diminishing sea ice in recent Arctic temperature amplification. *Nature*, **464**, 1334–1337, https://doi.org/10.1038/nature09051.

Serreze, M. C., and J. A. Francis, 2006: The Arctic amplification debate. *Climatic Change*, **76**, 241–264, https://doi.org/10.1007/s10584-005-9017-y.

Simmons, H. L., S. R. Jayne, L. C. St. Laurent, and A. J. Weaver, 2004: Tidally driven mixing in a numerical model of the ocean general circulation. *Ocean Modell.*, **6**, 245–263, https://doi.org/10.1016/S1463-5003(03)00011-8.

Speich, S., B. Blanke, and G. Madec, 2001: Warm and cold water routes of an O.G.C.M. thermohaline conveyor belt. *Geophys. Res. Lett.*, **28**, 311–314, https://doi.org/10.1029/2000GL011748.

——, ——, P. de Vries, S. Drijfhout, K. Döös, A. Ganachaud, and R. Marsh, 2002: Tasman leakage: A new route in the global ocean conveyor belt. *Geophys. Res. Lett.*, **29**, 1416, https://doi.org/10.1029/2001GL014586.

Stocker, T. F. and S. J. Johnsen, 2003: A minimum thermodynamic model for the bipolar seesaw. *Paleoceanography*, **18**, 1087, https://doi.org/10.1029/2003PA000920.

Stommel, H., and A. B. Arons, 1959: On the abyssal circulation of the world ocean—I. Stationary planetary flow patterns on a sphere. *Deep-Sea Res.*, **6**, 140–154, https://doi.org/10.1016/0146-6313(59)90065-6.

Talley, L. D., J. L. Reid, and P. E. Robbins, 2003: Data-based meridional overturning streamfunctions for the global ocean. *J. Climate*, **16**, 3213–3226, https://doi.org/10.1175/1520-0442(2003)016<3213:DMOSFT>2.0.CO;2.

Timmermann, A. and H. Goosse, 2004: Is the wind stress forcing essential for the meridional overturning circulation? *Geophys. Res. Lett.*, **31**, L04303, https://doi.org/10.1029/2003GL018777.

Toggweiler, J., and B. Samuels, 1995: Effect of Drake Passage on the global thermohaline circulation. *Deep-Sea Res. I*, **42**, 477–500, https://doi.org/10.1016/0967-0637(95)00012-U.

Vallis, G. K., 2006: *Atmospheric and Oceanic Fluid Dynamics: Fundamental and Large-Scale Circulation.* 1st ed. Cambridge University Press, 745 pp.

van Sebille, E., W. E. Johns, and L. M. Beal, 2012: Does the vorticity flux from Agulhas rings control the zonal pathway of NADW across the South Atlantic? *J. Geophys. Res.*, **117**, C05037, https://doi.org/10.1029/2011JC007684.

Veronis, G., 1975: The role of models in tracer studies. *Numerical Models of Ocean Circulation*, National Academy of Science, 133–146.

Warren, B. A., J. H. LaCasce, and P. E. Robbins, 1996: On the obscurantist physics of "form drag" in theorizing about the circumpolar current. *J. Phys. Oceanogr.*, **26**, 2297–2301, https://doi.org/10.1175/1520-0485(1996)026<2297:OTOPOD>2.0.CO;2.

Waterhouse, A. F., and Coauthors, 2014: Global patterns of diapycnal mixing from measurements of the turbulent dissipation rate. *J. Phys. Oceanogr.*, **44**, 1854–1872, https://doi.org/10.1175/JPO-D-13-0104.1.

Winton, M., 2003: On the climatic impact of ocean circulation. *J. Climate*, **16**, 2875–2889, https://doi.org/10.1175/1520-0442(2003)016<2875:OTCIOO>2.0.CO;2.

Zangenberg, N., and G. Siedler, 1998: Path of the North Atlantic Deep Water in the Brazil Basin. *J. Geophys. Res.*, **103**, 5419–5428, https://doi.org/10.1029/97JC03287.

Zika, J. D., M. H. England, and W. P. Sijp, 2012: The ocean circulation in thermohaline coordinates. *J. Phys. Oceanogr.*, **42**, 708–724, https://doi.org/10.1175/JPO-D-11-0139.1.